Astron. Astrophys. 252, 513–527 (1991)

ASTRONOMY AND ASTROPHYSICS

VLBI observations of 24 3CR CSS radio sources at 50 cm

Nan Rendong[1,2], R.T. Schilizzi[2], C. Fanti[3,4], and R. Fanti[3,4]

[1] Beijing Astronomical Observatory, Academia Sinica, Beijing 100080, China
[2] Netherlands Foundation for Research in Astronomy, Radiosterrenwacht Dwingeloo, Postbus 2, NL-7990 AA Dwingeloo, The Netherlands
[3] Dipartimento di Astronomia, Via Zamboni 33, I-40126 Bologna, Italy
[4] Istituto di Radioastronomia del CNR, Via Irnerio 46, I-40126 Bologna, Italy

Received January 4, accepted April 8, 1991

Abstract. We present the results of snapshot observations carried out at 50 cm with a Global VLBI Network on 24 compact steep-spectrum sources (CSS) from the 3CR catalogue (3C43, 48, 49, 67, 119, 138, 186, 190, 216, 237, 241, 268.3, 287, 298, 299, 303.1, 305.1, 309.1, 318, 343, 343.1, 346, 380, 454). The angular resolution ranges from about 20 mas for the global data to about 100 mas for the local networks (EVN and/or EVN+USVN) only. The minimum measurable surface brightness ranges from ≈ 10 to ≈ 40 mJy/beam.

Cores have been identified or confirmed in six sources (3C43, 186, 190, 216, 298, 346) through the spectral information contained in these observations. For radio components $\lesssim 150$ mas the new data allow the radio spectra to be evaluated down to 610 MHz. In general, no evidence is found for self-absorption, except in the radio cores.

Data reduction techniques have been developed to deal with the poor UV coverage of snapshot VLBI observations.

Key words: interferometry – galaxies – quasars – jets – CSS sources

1. Introduction

For some years we have been studying a representative set of compact steep-spectrum sources (CSSs) at several wavelengths and resolutions using the European and Global VLBI Networks, the MERLIN interferometer and the Very Large Array. The definition of the sample, and relevant references to our observing program can be found in Fanti et al. (1990), where a discussion of the properties of this class of sources is given.

This paper presents the results of a survey of the sample at 50 cm to obtain maps with dynamic range and resolutions comparable to those obtained at 18 cm and 6 cm using different VLBI arrays. The astrophysical motivation for these observations was to acquire spectral information across the source and to estimate the size of the individual radio components close to the low-frequency turnover in the integrated radio spectrum. In this initial survey of the structures at 50 cm we could not observe each source apparition fully due to restriction on the observation time. The resulting sparse UV coverage (see Sect. 2) restricts the size of the individual components which can be correctly reproduced in the image process to ≈ 150 mas. In practice, this has meant that we could obtain the desired information for about half of the sample.

The sources presented in this paper, with the addition of 3C147 and 3C286 studied at 50 cm by others (Wilkinson et al. 1977; Wilkinson & Readhead 1979; Kus et al. 1990), include all the sources from the revised 3CR catalogue (Jenkins et al. 1977) with radio luminosity greater than $10^{26.5}$ W Hz^{-1} at 178 MHz, and linear sizes less than 15 kpc ($H_0 = 100$ km s^{-1} Mpc^{-1}, $q_0 = 1$).

In this paper we present VLBI images at 50 cm for most of this sample; for 3C346 only the results from model fitting are given.

2. Observations and data reduction

The details of the sample are given in Table 1. The observations were made with telescopes at Torun (TORUN), Effelsberg (BONN), Westerbork (WSRT), Jodrell Bank (JBNK1), National Radio Astronomy Observatory (NRAO), North Liberty (IOWA), Fort Davis (FDVS), and Owens Valley Radio Observatory (OVRO) at 608 MHz (see Table 2), in left-circular polarization.

The observations covered the period 5–8 October 1986 (72 h). Two alternative modes of observation were employed for each 30 min scan: (1) the eight antennas in the global array all tracked the same object, (2) the two local networks (EVN and USVN) observed different objects when it was impossible to observe the same object simultaneously from the two continents. Each source was observed for about 3 h split into four to six snapshots spread over about a 10 h interval. Although this produces a sparse UV coverage, it is good enough to derive a reliable description of the main features of these sources. As a representative example we show the UV coverage of 3C48 in Fig. 1a.

The signals were recorded with the standard Mk2 VLBI system with 1.8 MHz bandwidth. The correlation was carried out on the 16-station JPL/Caltech correlator. Unfortunately, no fringes were detected on FDVS for unknown reasons. The data were further processed using the global fringe-fitting algorithm

Send offprint requests to: R. Fanti (Istituto di Radioastronomia)

Tables 1. The sample

Name	z^a	Id.^{b} (m_v)^c	Name	z^a	Id.^{b} (m_v)^c
3C43	1.46	Q (20.0)	3C287	1.06	Q (17.7)
3C48	0.37	Q (16.2)	3C298	1.44	Q (16.8)
3C49	0.62	G (22.0)	3C299	0.37	G (19.5)
3C67	0.31	G (18.0)	3C303.1	0.27	G (19.0)
3C119	0.41	Q (20.0)	3C305.1	1.13	G (21.0)
3C138	0.76	Q (17.9)	3C309.1	0.9	Q (16.8)
3C186	1.06	Q (17.6)	3C318	0.75	G (20.3)
3C190	1.2	Q (20.0)	3C343	0.99	Q (20.6)
3C216	0.67	Q (18.5)	3C343.1	0.75	G (20.8)
3C237	0.88	G (>21)	3C346	0.16	G (17.2)
3C241	1.62	G (>22)	3C380	0.69	Q (16.8)
3C268.3	0.37	G (17.3)	3C454	1.76	Q (18.5)

[a] Redshift; [b] Q = quasar, G = galaxy; [c] Visual magnitude

Table 2. Interferometer elements

Station name	Diameter (m)	System temperature	Sensitivity (K/Jy)
Jodrell Bank	76	100	1.0
Effelsberg	100	100	1.3
Westerbork	93[a]	120	1.0
Torun	15	130	0.03
Green Bank	43	60	0.21
Iowa	18	200	0.04
Owens Valley	40	95	0.28

[a] Equivalent diameter

(Schwab & Cotton 1983), which is implemented in the AIPS package and then coherently averaged for 30 s.

The data were calibrated according to the methods described by Cohen et al. (1975). The solutions for the calibration *b-factors* were made for each network separately because the calibrator, 0235+164, observed approximately every six hours, is slightly resolved on transatlantic baselines. Careful editing was carried out to remove bad data and the effects of possible interference.

The hole around the origin of the UV plane at baselines up to $\approx$0.4 million λ (Mλ) (see Fig. 1a) does not allow a circular gaussian source component with HPW greater than $\approx$150 mas to be reconstructed since it will be undersampled. In addition, the large gaps around 7 Mλ (the transatlantic gap) imply that components $\approx$30 mas from the brightest peak in the structure are not well constrained by the data in the *global* maps. The sparseness of the data causes confusion between the source structure and the prominent sidelobes, and limits the maximum size of the field that can be mapped. In the case of sparsely sampled data, individual telescope phase errors are poorly constrained by the self-calibration algorithms. Furthermore, even when these systematic errors are mostly removed, there remain spurious features (positive and negative), due to the large gaps in the UV plane, which overlay the source structure in most cases (see Fig. 1b).

In order to produce plausible maps, some considerable care had to be exercised in using VLBI data reduction software. This involved:

(1) Starting the mapping process for the simple sources with as accurate a model as possible. The generation of the models was based on the study of the visibility amplitudes in the UV plane and improved by means of the model-fitting algorithm in the CALTECH VLBI software package.

(2) Hybrid mapping with low resolution (EVN) data only, when the source structure is complex and, thus, difficult to describe by a few isolated gaussian features (e.g. 3C43, 119, 287 and 343). Subsequent addition of the USVN baselines and, whenever possible, the transatlantic baselines, allowed us to achieve a higher resolution.

(3) For complicated sources, using a priori information on the source structure, and deeper CLEANing with the AIPS package, using multi-windowing to constrain the area of sky in which the source structure is sought, with particular attention to those areas where components are visible at other frequencies.

(4) Evaluating the reliability of the results by blinking map and beam on the TV screen to determine the relative location of features in the maps and large sidelobes in the beam, to be sure that new features in the images are not spurious.

The visibility amplitudes and closure phases derived by Fourier transform of the CLEAN components were compared with the observed ones. They generally showed good fits. In principle, this does not guarantee that our solutions are the only possible ones. Nevertheless, the general agreement of our maps with the others obtained at different frequencies and/or resolutions confirms their reliability. We also show in the figures a few discrepant cases (e.g. 3C287, 3C305.1) to give an idea of the limits of mapping with very sparse UV data. As discussed in Sect. 4, however, these do not invalidate the main result we were aiming at, i.e. to compute the sizes and spectral indices of the source subcomponents, close to the low-frequency turnover in the spectrum.

The dynamic range achieved (defined as the ratio of peak brightness to rms noise level far from the source) is better than 100:1 in most cases; we do not claim, however, that this is the *fidelity level* of our maps.

The procedures involved are also described in Nan Rendong et al. (1990a).

3. Results

The final hybrid maps were analyzed to obtain the overall noise in the map and the component parameters. General information is given in Table 3. Here we report also the maximum observed visibility amplitude. The comparison of this value with the total flux density gives an estimate of the amount of signal which is present in structures too extended to be properly mapped with the present network. It is evident that baselines much shorter than 0.4 Mλ would be necessary in some cases to properly sample the extended features, but they are not presently available at 50 cm. Note that at 1.7 GHz, the frequency at which the sample has been observed systematically, this problem was solved by combining MERLIN data with the EVN.

Depending upon the source structure and complexity, different choices of synthesized beam size have been made in order to optimize the results in terms of resolution and dynamic range.

Eight of the 24 objects have been mapped with global data with resolutions ranging from $\approx 18 \times 10$ mas to $\approx 30 \times 20$ mas. A further seven sources have been mapped with EVN plus USVN

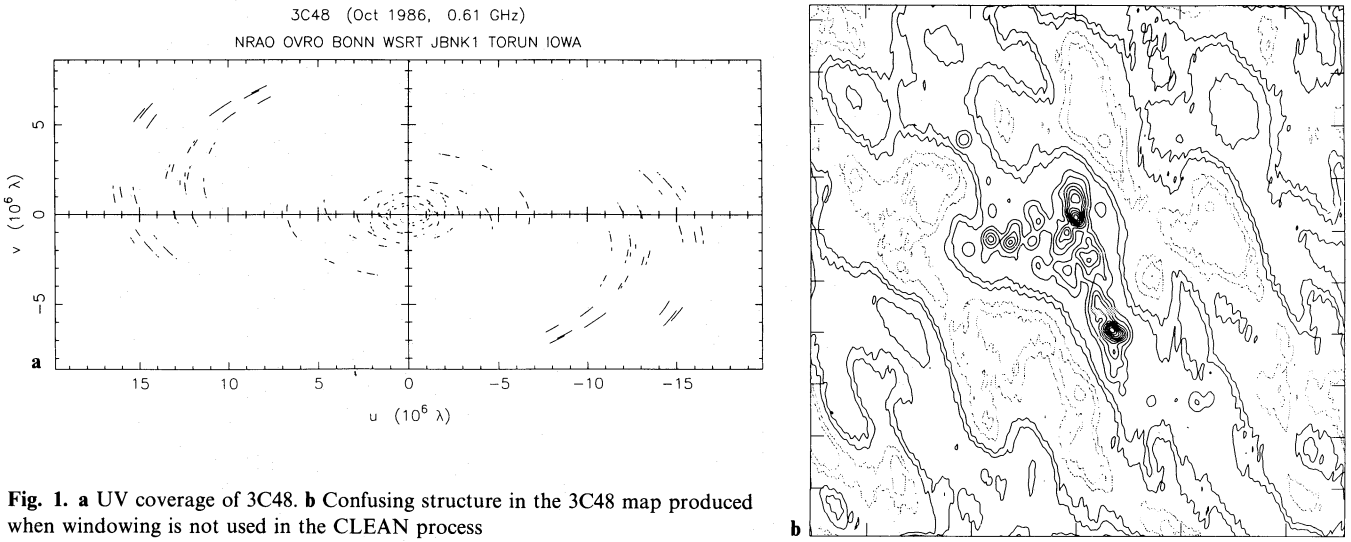

Fig. 1. **a** UV coverage of 3C48. **b** Confusing structure in the 3C48 map produced when windowing is not used in the CLEAN process

baselines, giving an average resolution of 60–80 mas. The remaining sources have EVN maps only (resolution 80–130 mas), except 3C346 whose structure could be studied only by model fitting due to the very limited amount of data.

Parameters of the source components are given in Table 4. Source subcomponents are labelled as explained in the notes to the table. As mentioned above, the flux densities of components larger than ≈ 150 mas will be underestimated (see also notes on individual sources). For those components whose flux densities at 0.6 GHz are considered reliable and for which flux densities at higher frequencies and with comparable resolutions are available from the literature (mostly van Breugel et al. 1984; Pearson et al. 1985; Akujor et al. 1991), we also give spectral indices (defined as $S \propto \nu^{-\alpha}$) in Table 4.

Table 3. Observational data

Fig. no.	3C name	VLBI[a] network	Peak flux (mJy/beam)	Noise (rms) (mJy/beam)	Flux in map (Jy)	Max. visib. ampl. (Jy)	Total flux[b] (Jy)
2	43	G	400	2.6	3.26	2.5	5.77
3	48	G	1600	4.9	16.27	14.5	31.46
4	49	G	1280	4.0	4.40	4.0	5.63
5	67	E	930	1.9	2.60	2.2	6.09
6	119	G	3590	5.2	12.70	12.0	14.10
7	138	E+U	4780	7.9	14.92	14.8	14.48
8	186	E	560	1.5	1.66	1.6	3.72
9	190	E	600	4.2	3.55	3.0	5.89
10	216	E+U	400	2.0	1.42	1.2	9.08
11	237	E	2600	5.9	9.99	8.3	12.77
12	241	E+U	1520	3.4	4.32	4.8	4.56
13	268.3	E	1860	1.4	5.62	5.1	7.56
14	287	G	2680	3.8	11.38	10.0	11.53
15	298	E+U	2220	6.6	9.98	8.2	16.38
16	299	E	640	1.4	2.00	1.8	6.38
17	303.1	E	1520	1.0	4.45	3.6	5.05
18	305.1	E	350	1.0	2.18	1.7	5.00
19	309.1	G	2200	6.0	8.60	7.8	14.00
20	318	E+U	1460	3.2	5.01	4.5	5.91
21	343	G	1500	4.0	10.25	9.25	11.12
22	343.1	E+U	1930	2.8	9.70	8.5	11.37
23	380	G	3130	9.0	6.26	6.6	28.51
24	454	E+U	1200	3.0	3.47	2.6	4.51

[a] G – Global network; E – EVN network; U – US network
[b] Total flux density, measured at WSRT simultaneously with VLBI observations

Table 4. VLBI data from the present paper

3C name	Total flux (Jy)	Source[a] comp.	VLBI flux (mJy)	Size (mas)	(p.a) deg.	Spectral index[b] 1. fr.	Spectral index[b] h. fr.
3C43	5.77	B	327	35 × 16	(1)	0.5	
		C	957	65 × 25	(177)	1.2[c]	
		D1	1064	37 × 17	(160)		0.7
		D2	450	27 × 12	(82)	1.1	
		E	397	32 × 11	(135)		
		F	160	20 × 9	(17)	1.0	
		G	50[c]	30 × 30[c]			
3C48	31.46	N1	3103	56 × 19	(173)		
		N2	1363	27 × 19	(85)		
		C	2682	66 × 30	(16)		
		S	3420	36 × 24	(16)		
		d	> 5700[c]	500 × 150[c]	(15)		
3C49	5.63	Ec	400	70 × 30	(45)	1.1	0.9
		Ed	> 600	150[c]			
		W	3100	30 × 15	(70)	0.7	0.9
3C67	6.09	N1	816	160 × 127	(121)		
		N2	156	145 × 17	(128)		
		S	1662	92 × 90	(74)		
3C119	14.10	A	4600	12 × 6	(178)	0.25	0.56
		B	1166	41 × 20	(156)	0.45	0.88
		C	3281[c]	50 × 50[c]		1.1	0.88
		E	2472[c]	100 × 60[c]			
3C138	14.48	E1	6830	65 × 37	(40)		
		E2	3050	86 × 33	(55)	0.6	0.6
		E3	1400	89 × 50	(46)		
		C	1631	40 × 24	(72)	0.75	0.0
		W	1809	160 × 81	(69)	0.7	
3C186	3.72	B	315	224 × 83	(70)		
		K	385	140 × 44	(162)		
		Ac	525	52 × 15	(15)		
		Ad	584	205 × 42	(71)		
3C190	5.89	D	1160	175 × 80	(107)	1.0	1.2
		A	1376	188 × 82	(98)	1.0	1.3
		B	978	unresolved		0.95	1.1
3C216	9.08	NE	505	190 × 35	(153)		
		SW1	565	93 × 52	(15)	0.6[c]	
		SW2	389	unresolved		0.0[c]	
3C237	12.77	E	4300	120 × 65	(80)		
		W	5600	130 × 90	(76)		
3C241	4.56	E	2205	59 × 29	(108)	1.3	1.6
		W1	1484	69 × 29	(113)	1.1	1.4
		W2	508	82 × 54	(74)	1.0	1.5
3C268.3	7.56	N	4450	118 × 81	(157)		
		S	1200[c]	190 × 110[c]	(54)		
3C287	11.53	C	8758	39 × 17	(90)		
		halo	2516[c]	150 × 100[c]			

Table 4 (continued)

3C name	Total flux (Jy)	Source[a] comp.	VLBI flux (mJy)	Size (mas)	(p.a) deg.	Spectral index[b]	
						1. fr.	h. fr.
3C298	16.38	A1	3714	87 × 67	(43)	1.4	1.9
		A2	751	223 × 14	(30)		
		B1	280	60 × 20	(131)	0.15	0.2
		B2	1643[c]	200 × 110[c]		1.0	1.0
		C1	1435	191 × 43	(89)		
		C2	2009	100 × 83	(48)	1.1	1.5
3C299	6.38	NE1	915	125 × 43	(46)		
		NE2	961	381 × 127	(62)		
		W	204[c]				
3C303.1	5.05	c	1116	unresolved		0.4	
		d	3114	213 × 118	(120)	1.6	1.6
3C305.1	5.00	N	1268[c]	500 × 124[c]	(26)		
		S	850[c]	500 × 100[c]	(75)		
3C309.1	14.00	E	2102[c]	200 × 200[c]			
		Cc	5609	32 × 8	(155)		
		Cd	934[c]	100 × 50[c]			
3C318	5.91	K3	756	62 × 43	(82)	1.3	1.6
		K2	1344	74 × 33	(44)	0.45	1.2
		A	2800	110 × 60	(147)	1.1	1.7
3C343	11.12	c	5004	39 × 18	(117)		
		d	5121[c]	200 × 120[c]			
3C343.1	11.37	E	3334	113 × 49	(124)	1.2	1.1
		W	6258	99 × 80	(67)	0.95	1.1
3C380	28.51	NW1	867	40 × 2	(111)		
		SE	4637	20 × 13	(127)	0.35	0.14
3C454	4.51	C	2418	175 × 21	(3)	0.65	0.7
		N	481	107 × 86	(145)	0.9	1.3
		S	519	173 × 70	(116)		0.8

[a] N1 means the northernmost, E1 the easternmost, etc.; C means the central; c, d mean compact and diffuse. Different labelling in multicomponent sources conforms to that used in other maps referred to in the text (mostly S91)

[b] 1. fr. refers to frequency range 0.6–1.7 GHz, and h. fr. to frequencies higher than 1.7 GHz

[c] The size is estimated from the lowest reliable contour and the flux density is obtained by integration; otherwise, the FWHM and flux density of the gaussian component best-fitting the map data (note that the two estimates of size differ by about a factor two). In both cases the size is deconvolved for the restoring beam

Hybrid maps for 23 sources are shown in Figs. 2–24. The synthesized beam sizes, peak flux densities, tick separations and contour values (in percentage of the peak flux density) are given in the figures captions.

4. Comments on individual sources

3C43 (Fig. 2): Maps with a resolution of a few tenths of an arcsec (Pearson et al. 1985; Spencer et al. 1989) show the source to have a markedly nonlinear triple structure extending over ≈2 arcsec. In the map at 50 cm, only the central component can be mapped, and its knotty structure seen in detail. The ≈40% of the total flux density missing in our map is undoubtedly to be found in the outer components which we resolve out. A map at 18 cm, with resolution similar to the present one, is given in Spencer et al. (1991) (hereafter referred to as S91). At that frequency the knots of the central component are embedded in low-brightness emission, which is not detected in our 50 cm observations due to the lack of short spacings, but is present in the 6 cm lower-resolution map of Akujor et al. (1991). The overall appearance of the knotty structure is similar in the two maps at 18 and 50 cm, but the individual knots show relative displacements of 10–20 mas. It is

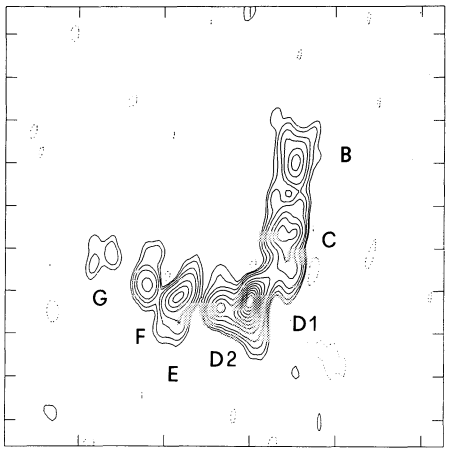

Fig. 2. 3C43 contours (%): −3, −1.5, 1.5, 3, 6, 10, 20, 30, 40, 50, 60, 70, 80, 90. Beam size 30 × 20 mas (10°); peak flux density: 0.40 Jy/beam; tick separation: 100 mas (X), 50 mas (Y)

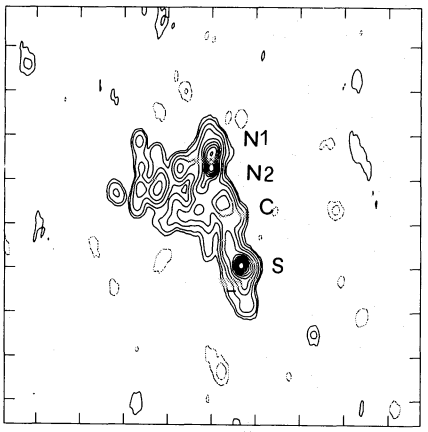

Fig. 3. 3C48 contours (%): −3, −2, −1, 1, 2, 5, 10, 20, 30, 40, 50, 60, 70, 80, 90. Beam size 30 × 20 mas (−10°); peak flux density: 1.6 Jy/beam; tick separation: 100 mas (X), 100 mas (Y)

unclear whether this is due to spectral effects or to the artefacts of CLEAN related to an inadequate UV coverage. The best overall agreement between the two maps is obtained by identifying the northernmost component in the 50 cm map with component B in S91. In this case we see that component A in S91 has no counterpart at 50 cm, implying a self-absorbed spectrum. It is very likely that this component is the source core. Component B in S91 has a flattish spectrum ($\alpha \approx 0.5$). The spectra of the other knots are uncertain, owing to the relative displacements of the knots at the two frequencies, but it seems most likely that all knots have a steep spectrum. The existence of the diffuse emission at 18 cm, not detected at 50 cm, makes more detailed comparisons uncertain.

3C48 (Fig. 3): The source structure at 50 cm is rather complex, containing a number of components embedded in lower-brightness emission. About 50% of the total flux density is missing, most likely in the extended component. There is good general agreement with the maps at 92 cm by Wilkinson et al. (1984) and Simon et al. (1990). Note, however, that the components N1, N2 and S at 610 MHz are brighter than at 327 MHz. This is found also by Wilkinson et al. (1990) using an unpublished 50 cm VLBI map. A low-brightness extension to the south has been detected in the region where a compact core is observed at 1.3 cm (Simon et al. 1990) and at 18 cm (Wilkinson et al. 1990). The whole structure is described by Wilkinson et al. (1990) as a jet flowing towards north and then spreading to the east.

3C49 (Fig. 4): The integrated flux density is ≈80% of that measured at WSRT. Parts of the diffuse emission in the 18 cm map of Fanti et al. (1985) (F85) are missing here due to the lack of short spacings. The western compact component has a spectral index ≈0.7 between 18 and 50 cm, indicating that the turnover in its spectrum suggested by Fanti et al. (1989) is at a frequency lower than the estimated one. The brighter NE fragment of the eastern component corresponds to the eastern hot spot in the 18 cm map, whose spectral index is ≈1.0.

3C67 (Fig. 5): The observations largely resolve out the structure; only ≈30% of the total flux density is seen in the BONN–WSRT baseline and <20% in the other baselines. The two main components are visible on all baselines. The northern low-brightness component is split into two regions which can also be seen at 18 cm (F85) and at 6 cm in Akujor et al. (1991). The bright compact part in the southern component is embedded in lower-brightness emission.

3C119 (Fig. 6): The high dynamic range image at 18 cm by Nan Rendong et al. (1991) reveals a complex spiral-like knotty structure. The core component, located 40 mas to the northeast of the B component, which is the brightest at all frequencies, is self-absorbed below 5 GHz (Fanti et al. 1986), consistent with the fact that we do not detect it at 50 cm. The most compact components at 18 and 6 cm, A and B (same labelling as in Fanti et al. 1986), appear to have a relatively flat spectrum in the frequency range 0.6–1.7 GHz. The detailed structure at 50 cm is not fully consistent with that at 18 cm. This is likely to be due to the sparseness of the UV data, especially to the large gap around 7 Mλ in the UV plane, which does not constrain the complex structure of the source well. Spectral effects across the source may also play a role.

3C138 (Fig. 7): The eastern part of the source structure has been clearly defined by the EVN at 18 cm (Geldzahler et al. 1984) and by MERLIN + EVN at 6 cm by Fanti et al. (1989). The central component in Fig. 7 (C in Table 4) corresponds to the western-most component on those maps. It has a spectral index of ≈0.75 between 18 and 50 cm, but the spectrum becomes flat around 10 GHz (see the high-frequency data of van Breugel et al. 1991a, in preparation). This component contains the source core. We confirm the existence of the western low-brightness extension visible in the MERLIN map at 6 cm (Fanti et al. 1989; Akujor et al. 1991).

3C186 (Fig. 8): Our map shows three main emitting regions, which account for only 40% of the total flux density. The component configuration is different to that seen in VLA observations at 2 cm (Cawthorne et al. 1986), but corresponds to structures seen in the 18 cm map (S91). The NW and SE components (labelled B and A, as in S91) are the brightest structures of the two symmetric lobes. The central component (K) is the brightest part of a one-sided jet. The source core, well visible

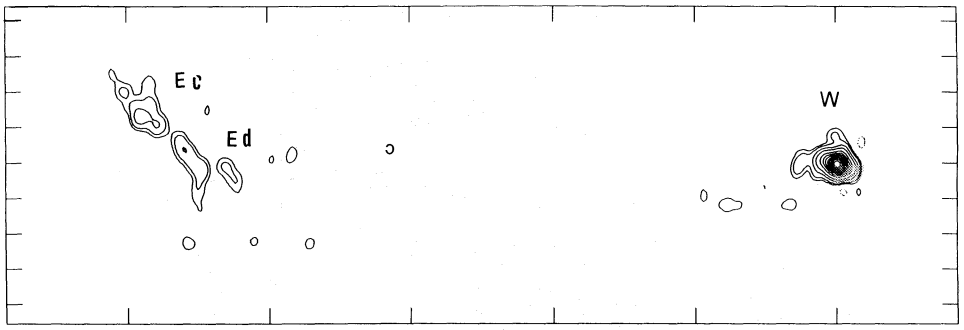

Fig. 4. 3C49 contours (%): −3, −2, −1, 1, 2, 5, 10, 20, 30, 40, 50, 60, 70, 80, 90. Beam size 30 × 20 mas (−10°); peak flux density: 1.28 Jy/beam; tick separation: 200 mas (X), 50 mas (Y)

in Cawthorne et al. (1986) as the brightest component, is completely self-absorbed here.

3C190 (Fig. 9): Our map (rotated by 45° CCW) shows three compact components whose separation and orientation are in good agreement with the VLA map at 2 cm (van Breugel et al. 1991a, in preparation). See also the combined MERLIN + EVN map at 18 cm in S91. A fourth component in the 2 cm VLA map, the brightest and most compact one, is absent at 50 cm (flux density <4 mJy), indicating that it is self-absorbed below 1 GHz, and suggesting that it is the core component. The three components have steep spectra ($\alpha \gtrsim 1.0$). The extended low-brightness emission visible at 5 GHz (Pearson et al. 1985) and at 1.7 GHz (S91) is not detected at 610 MHz due to the lack of short spacings.

3C216 (Fig. 10): The source is largely resolved even on the shortest baselines and the maximum correlated flux (JBNK1–WSRT) is only ≈13% of the total. VLA observations at 1.5 GHz display a low-brightness halo (Barthel et al. 1988; van Breugel et al. 1991a, in preparation) which accounts for 24% of

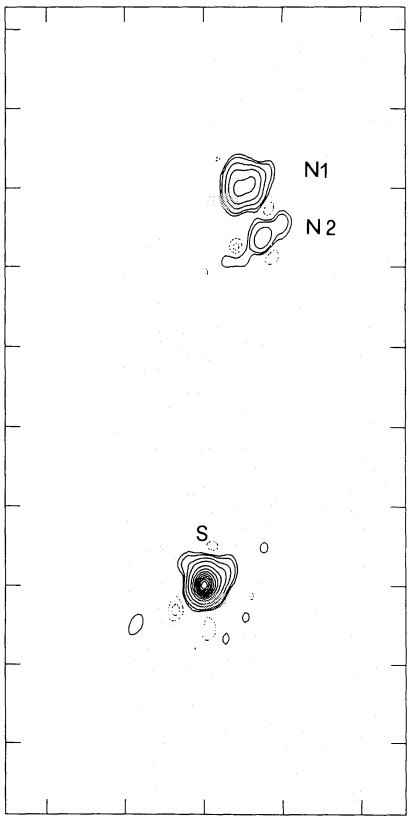

Fig. 5. 3C67 contours (%): −2, −1, 1, 2, 5, 10, 20, 30, 40, 50, 60, 70, 80, 90. Beam size 120 × 80 mas (−10°); peak flux density: 0.93 Jy/beam; tick separation: 500 mas (X), 500 mas (Y)

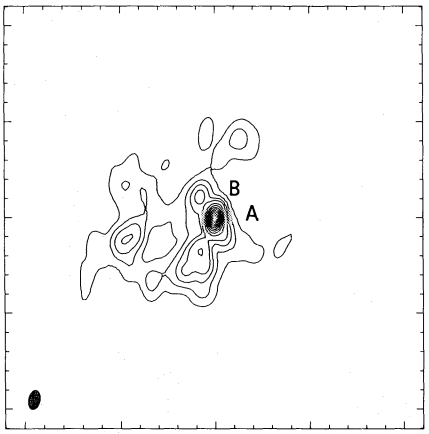

Fig. 6. 3C119 contours (%): −1, 1, 3, 6, 10, 20, 30, 40, 50, 60, 70, 80, 90. Beam size 20 × 12 mas (−10°); peak flux density: 3.59 Jy/beam; tick separation: 20 mas (X), 20 mas (Y)

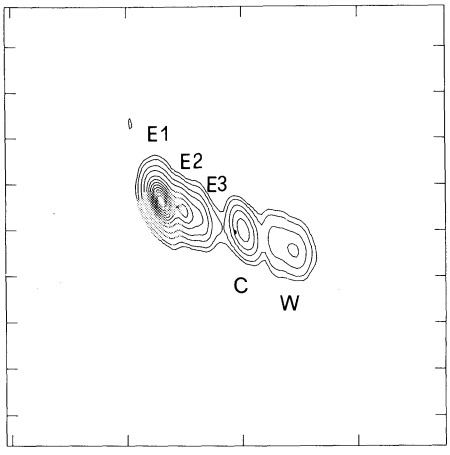

Fig. 7. 3C138 contours (%): −2, −1, 1, 2, 5, 10, 20, 30, 40, 50, 60, 70, 80, 90. Beam size 140 × 50 mas (15°); peak flux density: 4.78 Jy/beam; tick separation: 500 mas (X), 200 mas (Y)

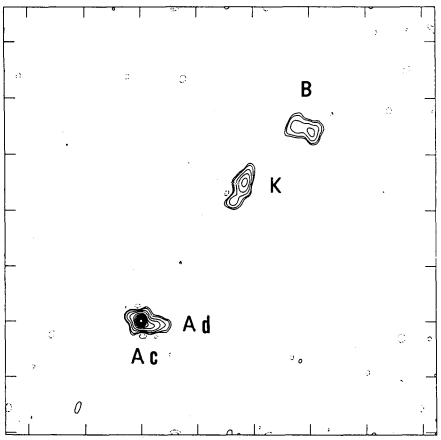

Fig. 8. 3C186 contours (%): −2, −1, 1, 2, 5, 10, 20, 30, 40, 50, 60, 70, 80, 90. Beam size 80 × 60 mas (−15°); peak flux density: 0.56 Jy/beam; tick separation: 500 mas (X), 500 mas (Y)

the total flux density. The bright central region is a triple (Pearson et al. 1985). Our 50 cm map shows the central and the northern components. The central components is resolved into two compact features, which may well be the source core (component SW2, with flat spectrum) and a bent jet linking it to the southern lobe, unseen here.

3C237 (Fig. 11): The source consists of two well-spaced edge-brightened components of similar flux density and size. The structure in the map accounts for ≈85% of the total flux density. The bright knot in the western component is even more elongated to the south than at 18 cm (F85).

3C241 (Fig. 12): The source is a double with comparable flux density in the two lobes. The western lobe is itself split into two parts, whose separation is the same as in the 18 cm map (F85) and in the 6 cm map by Akujor et al. 1991. The source has a weak (≈5 mJy) core visible only at frequencies greater than ≈5 GHz (Akujor et al. 1991; van Breugel et al. 1991a, in preparation). The flux density in the map is within a few percent of the single-dish measurement. The three components E, W1 and W2 have steep spectra: $\alpha = 1.4$, 1.1 and 1.0, respectively, between 0.6–1.7 GHz.

3C268.3 (Fig. 13): The source is a double with the same separation of ≈1.5 arcsec as in the 18 cm map (F85). Approximately 25% of the total flux density is missing in our map, most likely in the southern component, which is more diffuse. The northern component is barely resolved and its spectral index is ≈1.0 between 0.6 and 1.7 GHz.

3C287 (Fig. 14): The most detailed images of the source have been made from 6 cm VLBI data (Fanti et al. 1989) and from 18 cm VLBI data (Nan Rendong et al. 1988). It is a spiral-like structure similar to 3C119. The resolution of the present 50 cm map is not sufficient to resolve the bright central structure. The low-brightness features are not seen in the higher-frequency observations. They could be spurious due to insufficient UV coverage. If real, they should have a steep spectral index (see also the discussion in Sect. 5).

3C298 (Fig 15): In the 18 cm MERLIN map (Spencer et al. 1989) the source is a triple. About 50% of the total flux density is missing in our map, most likely in the diffuse components in the lobes. Four main features are seen in our 50 cm map, which are also visible in the high-frequency (>10 GHz) VLA maps (van Breugel et al. 1991a, in preparation). Component B1 corresponds to an unresolved component on the VLA high-frequency maps, on the VLBI 18 cm map by Graham & Matveyenko (1984), and on the 6 cm map by Akujor et al. 1991). Its spectrum peaks around 5 GHz, indicating that it is the location of the core. The other compact features (hot spots in the lobes) have steep spectra ($\alpha \gtrsim 1.0$). The complexity of the western lobe might not be real (e.g. Akujor et al. 1991), although hints of structure are visible also at 18 cm (Graham & Matveyenko 1985).

3C299 (Fig. 16): (map rotated by 25° CCW) Its structure was classified as complex by Fanti et al. (1990), because it was unclear whether a secondary component ≈12 arcsec to the SW was related to the main one. In the present map both components are seen. They are clearly extended along the line joining them, which suggests a real association. This is confirmed by recent VLA observations at 3.5 cm (van Breugel et al. 1991b, in preparation), which detect a faint radio core between these two components. The source is, thus, an asymmetric double of ≈40 kpc size and, to be consistent with the definition given in Sect. 1, it should be excluded from the CSS sample.

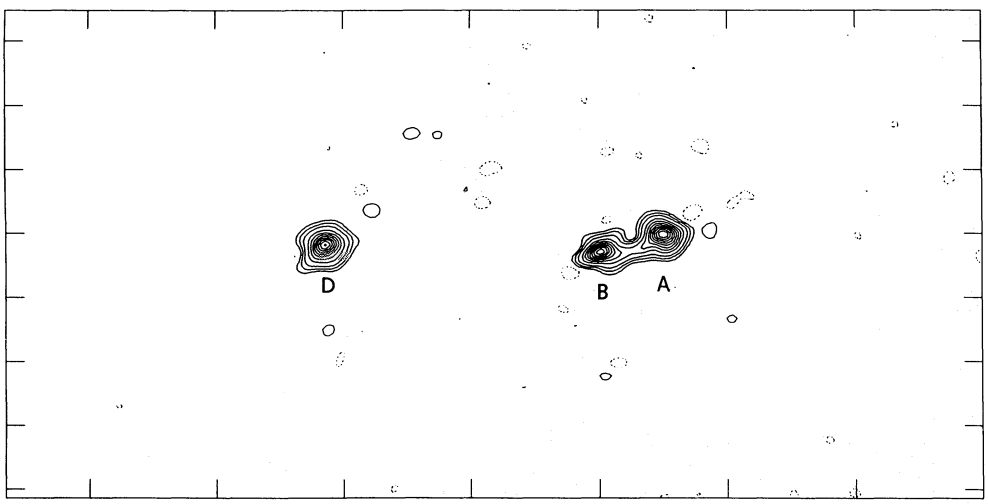

Fig. 9. 3C190 contours (%): −2, −1, 1, 2, 5, 10, 20, 30, 40, 50, 60, 70, 80, 90. Beam size 150 × 100 mas (60°); peak flux density: 0.60 Jy/ beam; tick separation: 1000 mas (X), 500 mas (Y). The map is rotated by 45° (CCW)

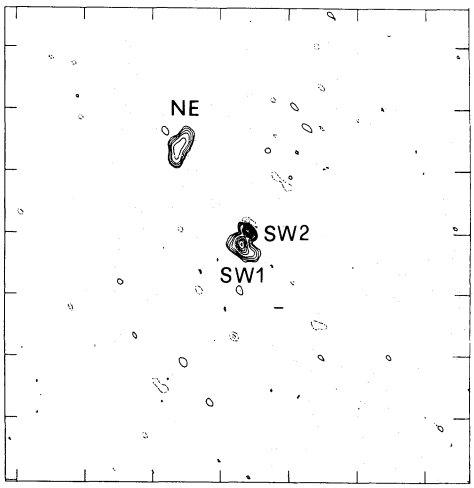

Fig. 10. 3C216 contours (%): −6, −3, −1.5, 1.5, 3, 6, 10, 20, 30, 40, 50, 60, 70, 80, 90. Beam size 80 × 50 mas (40°); peak flux density: 0.40 Jy/beam; tick separation: 500 mas (X), 500 mas (Y)

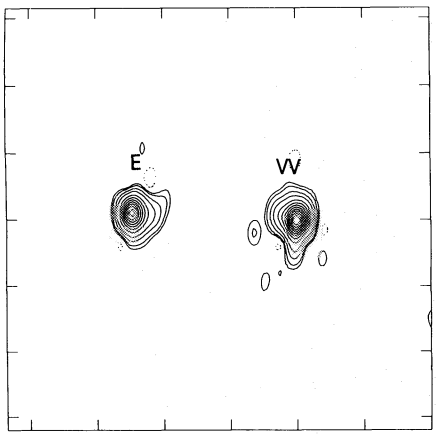

Fig. 11. 3C237 contours (%): −2, −1, 1, 2, 5, 10, 20, 30, 40, 50, 60, 70, 80, 90. Beam size 180 × 80 mas (−5°); peak flux density: 2.60 Jy/beam; tick separation: 500 mas (X), 500 mas (Y)

3C303.1 (Fig. 17): The map shows a single extended component which accounts for ≈ 70% of the total flux density of the source. A fainter component, visible at 1.8 arcsec in p.a. −41° in the MERLIN map at 1.7 GHz by Spencer et al. (1989) and in the 5 GHz VLA map by Pearson et al. (1985), is not detected here. Its flux density at 50 cm, extrapolated from the higher-frequency data accounts approximately for the missing flux density.

3C305.1 (Fig. 18): The source is largely resolved out even on the short baselines, accounting at most (BONN–WSRT) for 30% of the total flux density. It was in fact detected only on the baselines between WSRT, JBNK1 and BONN. The double structure is clearly seen in the limited UV data. The structure shown in the figure fits the UV data well, but the relative brightness of the components differs significantly from that in higher-frequency maps (e.g. Akujor et al. 1991; van Breugel et al. 1991a, in preparation). This is likely to be due to the very limited amount of data available to map this source, so we do not give in Table 4 any information other than the flux density and the size of the north and south main structures.

3C309.1 (Fig. 19): The overall structure of the source is clearly displayed in the VLA 5 GHz maps by van Breugel et al. (1984) and Pearson et al. (1985), where it appears as a bent triple. Higher-resolution maps at 6 cm with MERLIN and at 18 cm with EVN are given in Wilkinson et al. (1984) and Kus et al. (1990). About half of total flux density is missing in our map, very likely in the two extended lobes. The two components seen in our map are the central component of the triple and a bright feature in the eastern lobe. Their separation, orientation and extension are consistent with the higher-frequency maps (see also the 327 MHz VLBI map by Simon et al. 1990). A flat spectrum core, which has been found at 18 and 6 cm (Kus et al. 1990) just north of our western component, is unseen at 50 cm.

3C318 (Fig. 20): The source appears as a triple in a MERLIN map at 18 cm (S91). The southern component (A) in the 50 cm map is the southern lobe of the triple. The two close northern components (see also Akujor et al. 1991) correspond to knots in the central component seen at 18 cm. The northern lobe is not seen in our map.

3C343 (Fig. 21): The morphology is very complex. Our observations show a relatively bright halo which extends to the

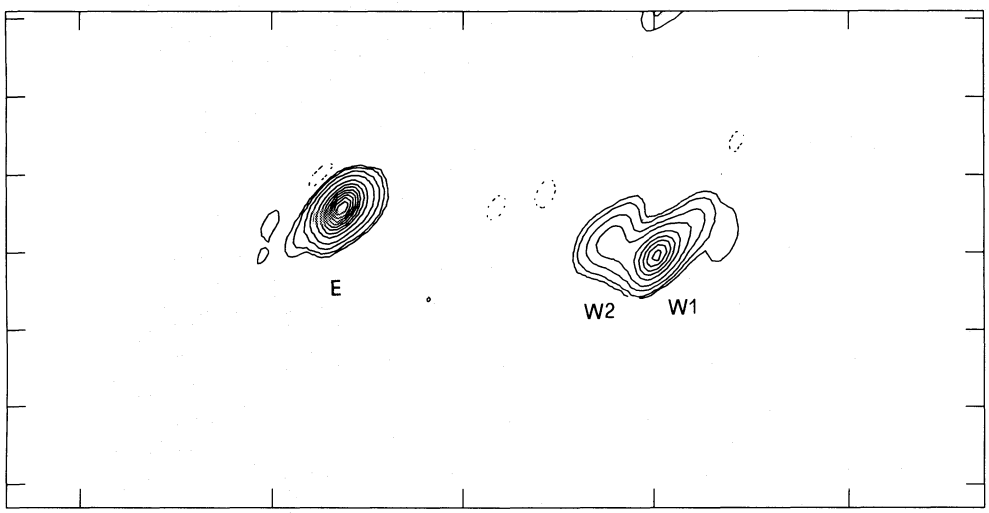

Fig. 12. 3C241 contours (%): −2, −1, 1, 2, 5, 10, 20, 30, 40, 50, 60, 70, 80, 90. Beam size 110 × 60 mas (−45°); peak flux density: 1.52 Jy/beam; tick separation: 500 mas (X), 200 mas (Y)

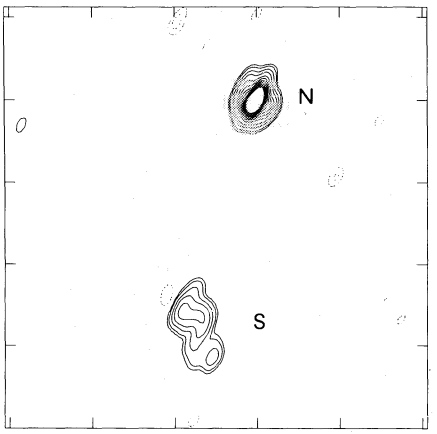

Fig. 13. 3C268.3 contours (%): (−2, −1, 1, 2, 5, 10, 20, 30, 40, 50, 60, 70, 80, 90) × 0.5. Beam size 110 × 60 mas (−45°); peak flux density: 1.86 Jy/beam; tick separation: 500 mas (X), 500 mas (Y)

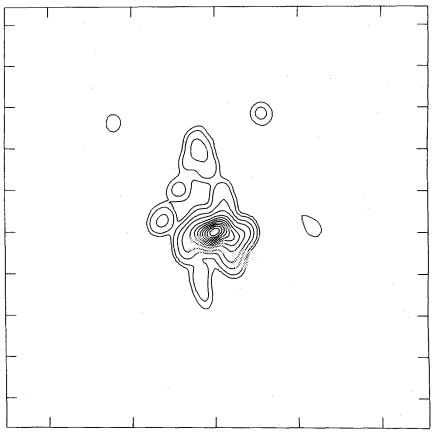

Fig. 14. 3C287 contours (%): −2, −1, 1, 2, 5, 10, 20, 30, 40, 50, 60, 70, 80, 90. Beam size 20 × 15 mas (−10°); peak flux density: 2.68 Jy/beam; tick separation: 100 mas (X), 50 mas (Y)

northwest in position angle $\approx -45°$, in agreement with a low-brightness feature in a global VLBI image at 18 cm by Schilizzi et al. 1991 (in preparation).

3C343.1 (Fig. 22): This is a double source with two differently shaped lobes. The map accounts for ≈90% of the total flux density. The two components have similar spectral indices: 1.16 for the eastern and 0.94 for the western component.

3C346 (no map): From VLA observations at 1.5 and 10.8 GHz (van Breugel et al. 1991a, in preparation) and MERLIN observations at 1.7 GHz (S91), the source appears as a *wide* double with a knotty one-sided jet and a bright flat spectrum core with flux density ≈200 mJy. In our observations the maximum correlated flux density is ≈6% of the total (on the BONN–WSRT baseline). The source structure derived from model fitting consists of two components with flux density 70 mJy (W) and ≈330 mJy (E) and 2.2 arcsec separation in position angle 80°. These two components correspond well to the source core and to the brightest knot in the jet. The spectral indices between 0.6 and 1.7 GHz for the knot in the jet and for the core are ≈0.5 and

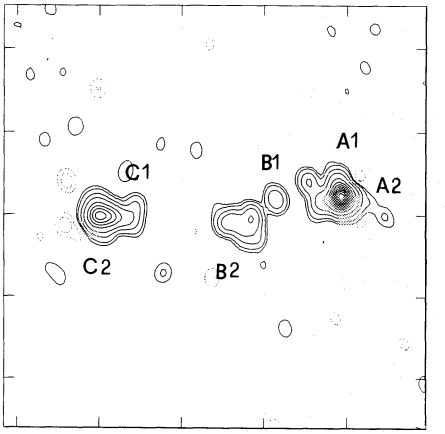

Fig. 15. 3C298 contours (%): −2, −1, 1, 2, 5, 10, 20, 30, 40, 50, 60, 70, 80, 90. Beam size 100 × 80 mas (−3°); peak flux density: 2.22 Jy/beam; tick separation: 500 mas (X), 500 mas (Y)

≈ −1.0, respectively. The core has, therefore, a highly inverted spectrum.

3C380 (Fig. 23): Only ≈20% of the total flux density is present in the map. The brightness distribution at 50 cm agrees with the compact features seen in the MERLIN + VLBI map at 18 cm by Wilkinson et al. (1984, 1991) and at 92 cm (Simon et al. 1990). The source core is located in the SE component (see the higher resolution map by Wilkinson et al. 1990 at 5 GHz) which is extended towards another compact component in the northwest (NW1), well visible also in Wilkinson et al. (1991). An elongated low-brightness feature is obviously related to the latter at an angle of ≈90° with respect to the source axis.

3C454 (Fig. 24): About 80% of the total flux density is contained in this map. The source has a triple morphology with a large bend angle (see also Cawthorne et al. 1986). The central component is resolved, and its knotty structure seen in greater detail by MERLIN + EVN observations at 18 cm (S91). The spectral indices between 0.6 and 1.7 GHz are ≈0.6 (Central), ≈0.9 (N) and ≈1.9 (S).

5. Discussion

5.1. Physical parameters

Physical parameters for the radio source components have been computed assuming equipartition and using standard formulae (Pacholczyk 1970). Proton and electron energies have been assumed equal, with a filling factor of unity. For each component an ellipsoidal geometry and the spectral index given in Table 4, over a frequency range from 10 MHz to 100 GHz, have been adopted. We have used the component sizes found at 50 cm.

Minimum total energy (U_{min}), minimum energy density (u_{min}) and equipartition magnetic field (H_{eq}) in the source components are:

$U_{min} \approx 10^{55}$–10^{57} erg,

$u_{min} \approx 10^{-6}$–10^{-7} erg cm^{-3},

$H_{eq} \approx 10^{-3}$–10^{-2} G,

in agreement with the earlier evaluations (Fanti et al. 1990).

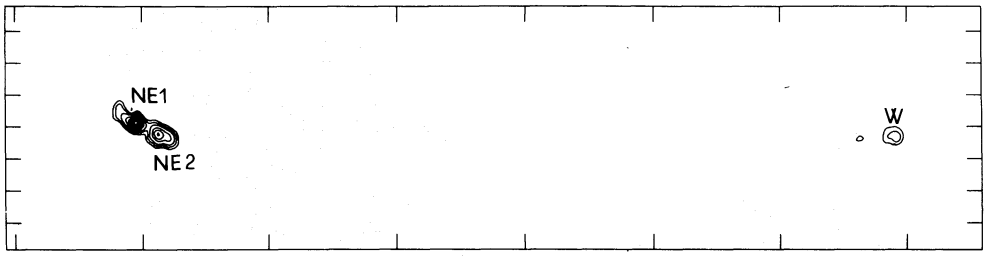

Fig. 16. 3C299 contours (%): −2, 2, 5, 10, 20, 30, 40, 50, 60, 70, 80, 90. Beam size 150 × 120 mas (−40°); peak flux density: 0.64 Jy/beam; tick separation: 2000 mas (X), 500 mas (Y). The map is rotated by 25° (CCW)

On the basis of the component sizes at 0.6 GHz, and assuming the equipartition magnetic field of the radio components, we have also computed the turnover frequencies for synchrotron self-absorption. These are generally well below 0.6 GHz, consistent with the finding (see next subsection) that the component spectra are generally straight down to that frequency. The angular sizes measured at 18 cm are often smaller and give turnovers at somewhat higher frequencies (30–40% higher) but still consistent with the data. Where this difference in size comes from is unclear; certainly, it cannot be attributed to a reduced surface brightness sensitivity at 18 cm, since the arrays used at this frequency have a better coverage of the shortest baselines than those at 50 cm (see Sect. 3). It is more likely to be due to the presence of steep spectrum extended features, better detected at the lower frequency.

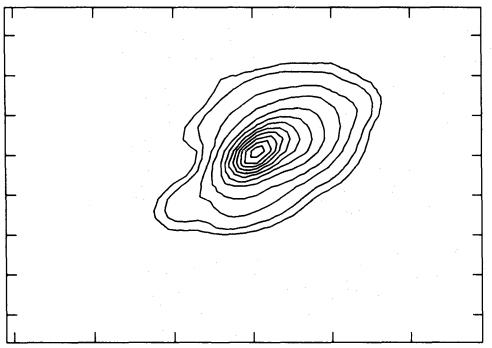

Fig. 17. 3C303.1 contours (%): −2, −1, 1, 2, 5, 10, 20, 30, 40, 50, 60, 70, 80, 90. Beam size 100 × 70 mas (−65°); peak flux density: 1.52 Jy/beam; tick separation: 200 mas (X), 100 mas (Y)

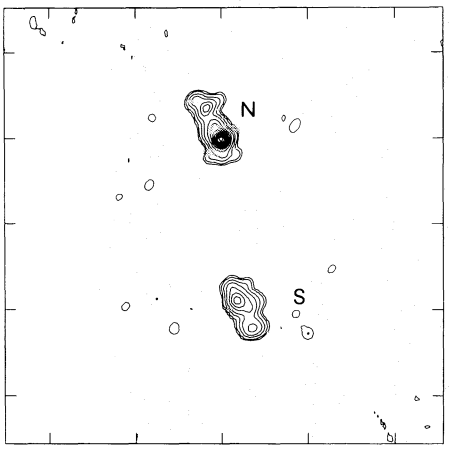

Fig. 18. 3C305.1 contours (%): −2, −1, 1, 2, 5, 10, 20, 30, 40, 50, 60, 70, 80, 90. Beam size 130 × 100 mas (−45°); peak flux density: 0.35 Jy/beam; tick separation: 1000 mas (X), 1000 mas (Y)

5.2. *Spectral analysis*

We have determined the spectral indices between 0.6 and 1.7 GHz for the radio components with sizes $\lesssim$150 mas (for which we believe we have reliable flux density measures) and have compared them with the high-frequency spectral indices, mostly from the VLA data (Pearson et al. 1985; van Breugel et al. 1991a, in preparation) and the MERLIN data (Akujor et al. 1991).

From this comparison we have identified or confirmed, the radio cores in six radio sources (3C43, 3C186, 3C190, 3C216, 3C298, 3C346). These radio cores are either undetected at 0.6 GHz, implying strong self-absorption, or are flat from 0.6 to 22 GHz. In 3C138 the core detected by Fanti et al. (1989) at 5 GHz is completely overwhelmed by the surrounding extended emission, when observed at 50 cm. For the remaining components, the spectral indices in the two frequency ranges (see Table 4) are reasonably consistent with each other, indicating that, except for components in 3C119 and 3C318, the spectra are transparent down to 0.6 GHz, consistent with the computed low-frequency turnovers for synchrotron self-absorption.

We have attempted a decomposition of the integrated source spectra in terms of the individual component spectra, under the hypothesis that the turnover is due to synchrotron self-absorption. To do this we have selected those sources in which our maps account for at least 75% of the 50 cm flux density. To this list we added 3C48, for which a comparison is possible between our map and that of Simon et al. (1990) at 327 MHz, and 3C43, for which our map well represents the central component. For each component of these sources we have derived the spectrum in the opaque regime using the spectral index given in Table 4 for the transparent frequency range and the computed low-frequency turnover, and adopting standard formulae (Pacholczyk 1970). Then we have compared the total spectrum of each source with the sum of the spectra of its components. Of course, the comparison between the observed and the computed spectrum constrains the parameters of the individual spectra most strongly at low frequencies ($\nu < 400$ MHz), when a clear indication of self-absorption is seen. There are, however, uncertainties in this comparison: (a) in several cases the low-frequency spectra are poorly known; (b) except in very few cases, we do not actually observe the low-frequency turnover in the individual components; (c) the computed turnover frequencies are quite sensitive to errors in the component sizes and these may be larger than expected (note also systematic differences between sizes measured at 50 and 18 cm).

In the following we comment on the sources for which we made the comparison.

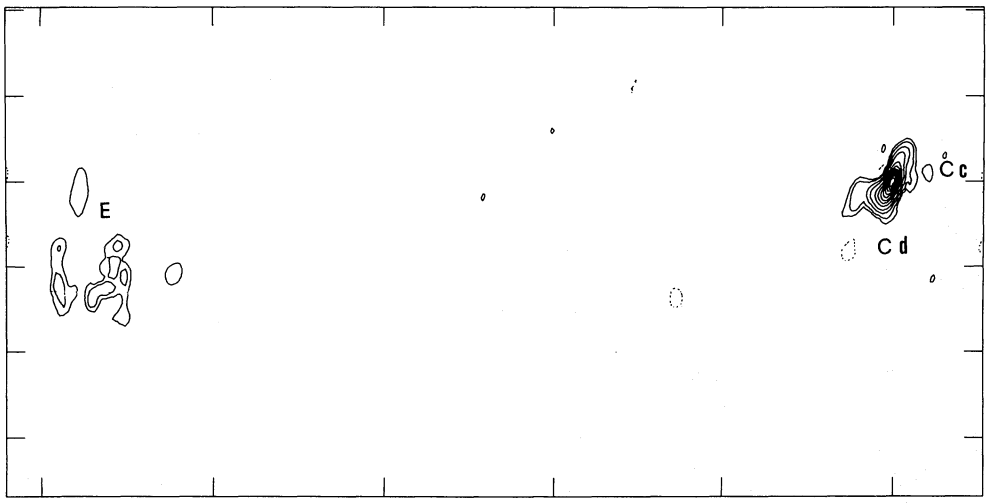

Fig. 19. 3C309.1 contours (%): −2, −1, 1, 2, 5, 10, 20, 30, 40, 50, 60, 70, 80, 90. Beam size 18 × 10 mas (−15°); peak flux density: 2.20 Jy/beam; tick separation: 200 mas (X), 100 mas (Y)

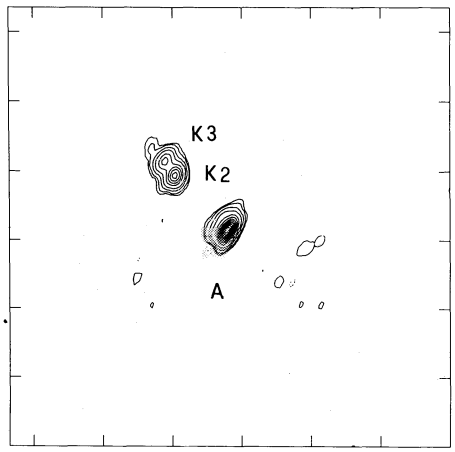

Fig. 20. 3C318 contours (%): −2, −1, 1, 2, 5, 10, 20, 30, 40, 50, 60, 70, 80, 90. Beam size 120 × 60 mas (−30°); peak flux density: 1.46 Jy/beam; tick separation: 500 mas (X), 500 mas (Y)

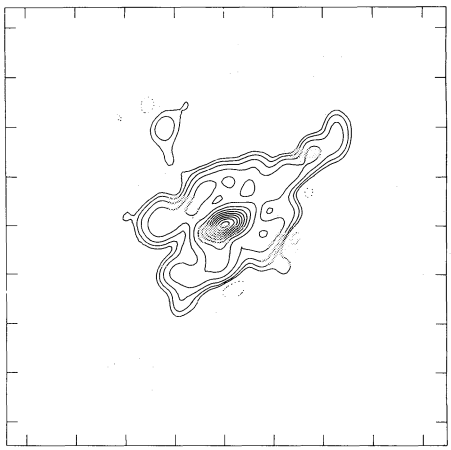

Fig. 21. 3C343 contours (%): −4, −2, −1, 1, 2, 4, 8, 15, 25, 35, 45, 55, 65, 75, 85, 95. Beam size 20 × 15 mas (−10°); peak flux density: 1.50 Jy/beam; tick separation: 50 mas (X), 50 mas (Y)

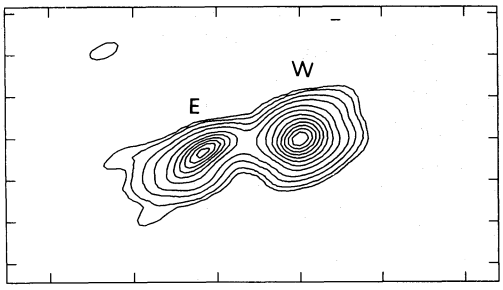

Fig. 22. 3C343.1 contours (%): −2, −1, 1, 2, 5, 10, 20, 30, 40, 50, 60, 70, 80, 90. Beam size 90 × 40 mas (−60°); peak flux density: 1.93 Jy/beam; tick separation: 200 mas (X), 100 mas (Y)

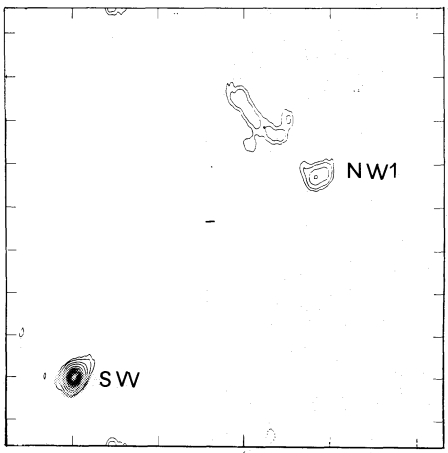

Fig. 23. 3C380 contours (%): −2, −1, 1, 2, 5, 10, 20, 30, 40, 50, 60, 70, 80, 90. Beam size 30 × 20 mas (−50°); peak flux density: 3.13 Jy/beam; tick separation: 400 mas (X), 100 mas (Y)

3C43: Extrapolation of the spectra of the two outer lobes shows that they would account for the total source flux density at ≈30 MHz. Subtracting the (extrapolated) flux density of the outer lobes from the total flux density allows us to derive the

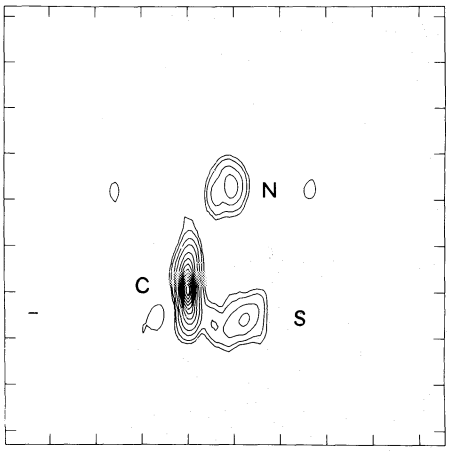

Fig. 24. 3C454 contours (%): −2, −1, 1, 2, 5, 10, 20, 30, 40, 50, 60, 70, 80, 90. Beam size 90 × 50 mas (0°); peak flux density: 1.20 Jy/beam; tick separation: 200 mas (X), 200 mas (Y)

spectrum of the central component. The difference spectrum flattens around 200–300 MHz. The flattening can be reproduced in the theoretical spectrum based on the computed self-absorption frequencies. Note, however, that there is a significant uncertainty in this procedure due to the imperfect matching of the 18 and 50 cm maps (sec Sect. 4).

3C48: The comparison of our map with that of Simon et al. (1990), which has a resolution very similar to ours, shows that components N1, N2 and S are less bright by a factor ≈ 1.35 at 327 MHz than at 610 MHz. Component C, instead, is brighter at 327 MHz. This implies that N1, N2 and S have turnover frequencies at ≈ 0.4 GHz, while for C the turnover frequency must be $\lesssim 0.2$ GHz. We note that the flattening in the total radio spectrum seen around 0.4 GHz is accounted for very well by the turnovers in components N1, N2 and S. These turnovers have been already noticed by Wilkinson et al. (1990), who suggest free–free absorption as explanation. Using our diameters measured at 0.6 GHz and the equipartition magnetic field we get a synchrotron self-absorption frequency $\lesssim 0.3$ GHz, not too far from the observed value. An exact agreement between the observed and the computed turnover frequencies would require a magnetic field ≈ 10 times larger than the equipartition value. Finally, we note that also the spectrum of the diffuse emission must turn over at $\lesssim 70$ MHz in order to justify the low-frequency spectrum at less than 0.1 GHz. This may not be inconsistent with the observed brightness and equipartition magnetic field in terms of synchrotron self-absorption.

3C49: The high-frequency spectra of the components and the computed turnover frequencies allow the overall spectrum to be reproduced quite well.

3C119: Components A and B are clearly self-absorbed and the available flux densities are well fitted by a self-absorbed spectrum. This allows one to determine the turnover frequencies directly and to compare them with the computed values. For component B we find $\nu_{max} \approx 0.5$ GHz, in fair agreement with the computed value (the size measured at 18 cm gives the best agreement). For component A the observed value (≈ 0.6 GHz) is lower than the expected. The agreement would require either a component size much larger than seen or a magnetic field an order of magnitude fainter than the equipartition value. Note that there is some uncertainty in the measured sizes; they seem to increase systematically with wavelength from 6 to 50 cm and interstellar scattering has been suggested as an explanation (Fanti et al. 1986). The overall spectral flattening at ≈ 0.4 GHz is accounted for by the turnovers of A and B. The lower-frequency part of the spectrum can also be fitted, but it is poorly constrained due to insufficient data on the more extended components.

3C138: Although we have no direct evidence of absorption in the individual components down to 0.6 GHz, we can reproduce the total spectrum on the basis of computed turnover frequencies of the individual components. In particular, the flattening at 250 MHz is fully accounted for by the components E1, E2, E3 (we use the 6 cm sizes given in Fanti et al. 1989). The reproduction of the spectrum at lower frequencies is poorly constrained by the available data on the more diffuse emission, which should turn over at ≈ 100 MHz.

3C237: The two components have substructures (see 18 cm map in F85) which justify turnover frequencies between 80 and 150 MHz. The computed total spectrum turns over in the right range but is too sharply peaked compared to the observations.

3C241: This is an excellent test case, since the total flux density is well accounted for by our maps at 0.6 and 1.7 GHz. Furthermore, there is quite a good agreement between the angular sizes measured at the two frequencies and no significant extended emission seems to be present. The spectra of the three components are expected to turn over between 0.2 and 0.3 GHz. The overall computed spectrum fits the data well down to 178 MHz. Then it turns down sharply, but no data are available for comparison at lower frequencies.

3C268.3: The spectra of the radio components are expected to turn over between 80 and 150 MHz. The total spectrum is not well known below ≈ 200 MHz.

3C287: The spectrum of the brighter emission region is expected to turn over at ≈ 0.5 GHz, close to the frequency where the total spectrum flattens. However, the observed spectrum has a very broad maximum which extends down to ≈ 50 MHz. In order to reproduce it, lower-brightness emission is required, evidence for which is seen in our map.

3C303.1: The spectra of the diffuse and compact components are expected to turn over at ≈ 0.1 and 0.2 GHz, respectively. Inclusion of the secondary component at ≈ 1.8 arcsec (not detected in our map) allows the total flux density to be reproduced. The relatively flat spectrum of the compact component at low frequencies is not clearly due to self-absorption on the basis of our measured angular sizes and the equipartition magnetic field. Moreover, since the high-frequency spectral behaviour of this component is unknown, it is not clear that self-absorption occurs.

3C318: Component K2 seems self-absorbed at 0.6 GHz. This is much higher than the computed turnover frequency.

3C343: The spectrum of the brighter component at 0.6 GHz is expected to turnover at ≈ 0.4 GHz, the frequency at which the overall spectrum begins to flatten. In view of the very complex structure of this source (Schilizzi et al. 1991, in preparation), we have not attempted a detailed spectral fit.

3C343.1: Frequency turnovers are expected in the range 0.15–0.25 GHz. However, the computed spectrum appears too sharply peaked with respect to the observed one.

3C454: The spectrum of the central component is expected to turn over at frequencies $\lesssim 0.2$ GHz. The overall spectrum is straight and may be reproduced without difficulty, but it is poorly constrained by the extended emission (components N and S).

6. Conclusions

We summarize the main results as follows:

(a) The paper presents maps of 23 3CR CSSs from the sample defined in Fanti et al. (1990), obtained at 50 cm from snapshot observations with a global VLBI array. In spite of the limited data, the maps have dynamic ranges of typically 100:1 and enable us to study radio components with angular size $\lesssim 150$ mas. Components with larger sizes are poorly mapped due to limitations in the UV coverage of the VLBI network used. For this reason it is not possible to make a morphological classification based on the present data alone. Nevertheless, these data confirm the classification given in Fanti et al. (1990), based on MERLIN and VLBI data at higher frequencies. The angular sizes measured at 50 cm tend to be larger, by a factor of ≈ 1.5, than those found at 18 cm (F85 and S91). Whether this is a genuine property of the sources or a spurious effect due to the lower quality of the low-frequency data is not possible to assess at the moment.

(b) From comparisons with higher-frequency maps (either VLBI at 1.7 GHz, Merlin at 5 GHz, or VLA at 15 and 22 GHz) we have identified or confirmed the radio cores in six radio sources (3C43, 3C186, 3C190, 3C216, 3C298, 3C346). These radio cores are either undetected at 0.6 GHz, implying strong self-absorption, or are flat from 0.6 to 22 GHz. In the case of 3C138, the core detected by Fanti et al. (1989) at 5 GHz is completely overwhelmed by extended emission, unresolved at 50 cm.

(c) We have determined the spectral indices between 0.6 and 1.7 GHz for radio components with sizes $\lesssim 150$ mas at 50 cm (for which we believe we have good flux density measures) and compared them with the high-frequency spectral indices from the Merlin (Akujor et al. 1991) and VLA data (van Breugel et al. 1991a, in preparation). The spectral indices in the two frequency ranges (see Table 4) are reasonably consistent with each other, indicating that, except for subcomponents in 3C119 and 3C318, the spectra are transparent down to 0.6 GHz. We have tried to reproduce the total spectra of the sources in terms of synchrotron self-absorbed spectra of the individual components. For this the low-frequency turnovers have been computed from the observed component brightness and from the equipartition magnetic fields. In general, the agreement is good, but some discrepancies are found and discussed. We stress that this analysis does not constrain the magnetic field intensity any better than within a factor of ten.

More detailed study of the low-frequency spectra and better-determined component sizes at frequencies as close as possible to the turnover frequency are required in order to determine the physical parameters with greater accuracy.

Acknowledgements. Nan Rendong is supported by a grant from the National Natural Science Foundation in China. He also acknowledges the hospitality provided by the Dwingeloo Observatory and the Bologna Institute of Radio Astronomy during his visits made in 1987 and 1988. The authors thank Dr. Barthel, Dr. Unwin and the staff of the Caltech/JPL VLBI correlator for their precious support during the processing of the data. They also thank the staff of the various observatories for carrying out the observations. The Netherlands Foundation for Research in Astronomy is supported by the Netherlands Organization for Scientific Research (NWO).

References

Akujor C.E., Spencer R.E., Zhang F.J., Davis R.J., Browne I.A.W., Fanti C., 1991, MNRAS 250, 214
Barthel P.D., Pearson T.J., Readhead A.C.S., 1988, ApJ 329, L51
Cawthorne T.V., Scheuer P.A.G., Morrison I., Muxlow T.W.B., 1986, MNRAS 219, 883
Cohen M.H., Moffet A.T., Romney J.D., Schilizzi R.T., Shaffer D.B., Kellermann K.I., Purcell G.H., Grove G., Swenson G.W., Yen J.L., Pauliny-Toth I.I.K., Preuss E., Witzel A., Graham D., 1975, ApJ 201, 249
Fanti C., Fanti R., Parma P., Schilizzi R.T., van Breugel W.J.M., 1985, A&A 143, 292 (F85)
Fanti C., Fanti R., Schilizzi R.T., Spencer R.E., van Breugel W.J.M., 1986, A&A 170, 10
Fanti C., Fanti R., Parma P., Venturi T., Schilizzi R.T., Nan Rendong, Spencer R.E., Muxlow T.W.B., van Breugel W.J.M., 1989, A&A 217, 44
Fanti R., Fanti C., Schilizzi R.T., Spencer R.E., Nan Rendong, Parma P., van Breugel W.J.M., Venturi T., 1990, A&A 231, 333
Geldzahler B.J., Fanti C., Fanti R., Schilizzi R.T., Weiler K.W., Shaffer D.B., 1984, A&A 131, 232
Graham D.A., Matveyenko L.I., 1984, IAU Symp. 110. VLBI and Compact Radio Sources, eds. Fanti, Kellermann, Setti, Reidel, Dordrecht, p. 43
Kus A.J., Wilkinson P.N., Pearson T.J., Readhead A.C.S., 1990, Workshop on Parsec scale radio jets, eds. Pearson, Zensus, Cambridge Univ. Press, Cambridge, p. 161
Jenkins C.J., Pooley G.G., Riley J.M., 1977, Mem. R. Astron. Soc. 84, 61
Nan Rendong, Schilizzi R.T., Fanti C., Fanti R., van Breugel W.J.M., Muxlow T.W., 1988, IAU Symp. 129. The Impact of VLBI on Astrophysics and Geophysics, eds. Reid, Moran, p. 119
Nan Rendong, Schilizzi R.T., Fanti C., Fanti R., Deng Jie, 1990a, China Science 34, 590
Nan Rendong, Schilizzi R.T., van Breugel W.J.M., Fanti C., Fanti R., Muxlow T.W., Spencer R.E., 1991, A&A (in press)
Pacholczyk A.G., 1970, Radio Astrophysics, Freeman, San Francisco
Pearson T.J., Perley R.A., Readhead A.C.S., 1985, AJ 90, 738
Schwab F.R., Cotton W.D., 1983, AJ 88, 688
Simon R.S., Readhead A.C.S., Moffet A.T., Wilkinson P.N., Booth R., Allen B., Burke B.F., 1990, ApJ 354, 140
Spencer R.E., McDowell J.C., Charlesworth M., Fanti C., Parma P., Peacock J.A., 1989, MNRAS 240, 657
Spencer R.E., Schilizzi R.T., Fanti C., Fanti R., Parma P., van Breugel W.J.M., Venturi T., Muxlow T.W.B., Nan Rendong, 1991, MNRAS 250, 225 (S91)

van Breugel W.J.M., Miley G.K., Heckman T.A., 1984, AJ 89, 5
Wilkinson P.N., Readhead A.C.S., Purcell G.K., Anderson B., 1977, Nat 269, 764
Wilkinson P.N., Readhead A.C.S., 1979, ApJ 232, 365
Wilkinson P.N., Spencer R.E., Readhead A.C.S., Pearson T.J., Simon R.S., 1984, IAU Symp. 110. VLBI and Compact Radio Sources, eds. Fanti, Kellermann, Setti, Reidel, Dordrecht, p. 25
Wilkinson P.N., Tzoumis A.K., Akujor C.E., Benson J.M., Walker R.C., Simon R.S., 1990, Workshop on Parsec scale radio jets, eds. Zensus, Pearson, Cambridge Univ. Press, Cambridge, p. 152
Wilkinson P.N., Akujor Chidi E., Cornwell T.J., Saikia D.J., 1991, MNRAS 248, 86